Proceedings of ASME Turbo Expo 2011
GT2011
June 6-10, 2011, Vancouver, British Columbia, Canada

GT2011-45891

THE EFFECTS OF BLADE LOADING ON TRAILING EDGE VORTEX FORMATION ON A HIGHLY LOADED STATOR UPSTREAM OF A TRANSONIC ROTOR

Kenneth P. Clark
Steven E. Gorrell
Department of Mechanical Engineering
Brigham Young University
Provo, Utah 84602

ABSTRACT

Multiple high-fidelity time-accurate computational fluid dynamics simulations were performed to investigate the effects of upstream stator loading and rotor shock strength on vortex shedding characteristics in a single stage transonic compressor. Three loadings on the upstream stator row of decreased, nominal, and increased were studied. The time-accurate URANS code TURBO was used to generate periodic, quarter annulus simulations of the Blade Row Interaction compressor rig. It was observed that vortex shedding was synchronized to the passing of a rotor bow shock. Results show that vortex size and strength increase with stator loading. "Normal" and "large" shock-induced vortices formed on the stator trailing edge immediately after the shock passing, but the "large" vortices were strengthened at the trailing edge due to a low velocity region at the suction surface. This low velocity region was generated upstream on the suction surface from a shock-induced thickening of the boundary layer or separation bubble. The circulation of the "large" vortices was greater than the "normal" vortices by a factor of 1.7, 1.9 and 2.1 for decreased, nominal and increased deswirler loadings. At decreased loading only 24% of the measured vortices were considered "large" while at nominal loading 58% were "large". An understanding of the unsteady interactions associated with blade loading and rotor shock strength in transonic stages will help compressor designers account for unsteady flow physics at design and off-design operating conditions.

NOMENCLATURE

AFRL	Air Force Research Laboratory
SMI	Stage Matching Investigation
BRI	Blade Row Interaction
WG	Wake Generator
IGV	Inlet Guide Vane
TE	Trailing Edge
PIV	Particle Image Velocimetry
NL	Nominal Loading
DL	Decreased Loading
IL	Increased Loading
C_p	Pressure Coefficient, $C_p = \frac{P-\overline{P_1}}{\overline{P_{01}}-\overline{P_1}}$
ω_r	Radial Vorticity
Γ	Circulation
U	Axial Velocity
V	Tangential Velocity

INTRODUCTION

High speed, high performance turbomachines typically are designed with highly loaded blade rows with decreased axial spacing, thereby exhibiting significant unsteady losses between blade rows not observed in low-speed turbomachines. These blade-row interactions, such as the interaction of a shock with a blade surface or a blade wake, are a significant source of unsteadiness in high-speed turbomachines. Most contemporary compressor design tools do not directly account for these signif-

icant unsteady effects. A better understanding of such phenomena is needed to identify the impact of unsteady aerodynamics on compressor performance, to develop and validate tools for measuring and modeling unsteady flows and to develop design tools that more accurately account for unsteady aerodynamics.

Three dimensional experiments and computational simulations are necessary to accurately predict compressor performance, especially in the transonic regime where the rotor leading edge shock accounts for the majority of the pressure rise and loss. Adamczyk [1] described the need for experimental and numerical work which focused on unsteady fluid mechanics and the impact on axial turbomachinery performance. Experimental results increase understanding of these unsteady flows and can also be used to verify results obtained from design tools. Adamczyk described a need for multi-stage design tools that do not rely on empirical formulations or data as inputs. He showed that in order to develop design tools that account for unsteady characteristics, a more complete understanding of unsteady flows that are classified as nondeterministic but are not turbulent in nature must be obtained. An example of these unsteady flow characteristics is the shedding of vortices from a blade's trailing edge.

Vortex shedding in turbomachines has been the focus of research for some time. Hathaway et al. [2] observed vortex shedding in fan rotors, which were shown to lead to spanwise redistribution of entropy by Kotidis and Epstein [3]. It has also been observed that the stretching of vortices leads to flow instabilities which resulted in rapid mixing [4]. These unsteady non-turbulent flows appear to lead to the mixing of shear layers and therefore generate loss which reduces pressure rise and efficiency.

The impact of such mixing processes on aerodynamic performance of multistage axial flow turbomachines was initially accomplished using low-speed compressor experiments. For subsonic compressor stages higher efficiency and pressure rise were observed with decreased axial spacing. This trend is not observed in transonic rotors due to important blade row interactions present in high speed rotors. In subsonic compressors, wake recovery [1, 5–9] has been shown to be the mechanism responsible for increased efficiency at reduced rotor-stator axial spacing. Though wake recovery could theoretically reduce wake mixing loss for transonic compressor stages, there are additional interactions that occur between blade rows, such as wake-shock and shock-vortex interactions. It is because of such transonic unsteady interactions that as axial spacing is reduced other major sources of loss are incurred. These unforeseen and unquantified blade row interactions result in performance much lower than design expectations for some transonic compressors. An understanding of these high speed blade row interactions will help designers more accurately predict true compressor performance in the transonic regime.

Prior experimental and computational transonic blade row interaction research has discovered how the interaction of a rotor bow shock with an upstream stator trailing edge generates additional loss. It was found that decreased axial spacing generated loss-producing blade row interactions not seen in low-speed compressors. Rig tests [6, 10, 11] have shown that when stator-rotor axial spacing was reduced the pressure ratio, mass flow rate, and efficiency all decreased. Analysis [12–14] showed that shed vortices increase in size and strength with rotor bow shock strength, leading to more incurred loss with decreased axial gap. The formation of the vortex was found to correlate with the rotor bow shock passing. Vortices were shed from the trailing edge of the upstream stator in response to the unsteady, discontinuous pressure field generated by the downstream rotor bow shock.

In transonic compressors Ottavy et al. [15] performed measurements and analysis on the interaction between the rotor bow shock and the wake shed from an Inlet Guide Vane (IGV). The experiment used laser two-focus anemometer measurements between an IGV and transonic rotor. The results showed that the shock wave had a large effect on the wake. Upstream of the shock wave the wake depth was reduced and the wake was overturned as a result of an expansion zone in the flow due to the curvature of the rotor blade suction surface. Downstream of the shock wave the wake-deficit increased and the wake was underturned.

Sanders and Fleeter [16], performed PIV measurements on the wake shed from an IGV in a transonic compressor. Their results demonstrated oblique shock effects in the upstream blade row, shedding and boundary layer separation, and the unsteadiness in the upstream blade row was driven by the downstream rotor. The Blade Row Interaction (BRI) rig simulated an embedded transonic fan stage that produced a wake through diffusion (viscous effects) with realistic geometry. The BRI rig was designed to not only vary the stator-to-rotor axial spacing but the stator loading as well. Both experimental and computational methods were used to analyze the BRI rig.

Reynolds [17] sought to determine the effects of upstream stator loading and rotor bow shock strength on the strength and size of shed vortices through experimental PIV work. It was observed that vortex shedding was synchronized to the passing of the rotor bow shock, with two strong vortices shed due to the passing shock, followed by a smaller shed vortex due to natural shedding effects. The data showed that the circulation of a vortex increased by 19% from far to mid, and 23% from mid to close spacing due to the increased strength of the rotor bow shock impacting the stator trailing edge. Reduction in upstream stator loading caused a decrease in shed vortex circulation for the same stator/rotor axial spacing by 20 to 25%.

Motivation

This paper continues to investigate the effect of stator loading on shed vortices in greater detail. The PIV measurements cited in [17] did not capture the stator suction surface flow field. Understanding the challenges and consequences of stator load-

ing variations, thick boundary layers, or possible separation on the suction surface has not previously been investigated and will be shown to be of great importance. This research illustrates for the first time what happens to the size and strength of shed vortices in highly loaded blade rows and at off-design operating conditions due to varying stator incidence. High-fidelity, time-accurate CFD simulations at three different stator loadings allow a more thorough analysis of the cause as well as the effect of stator loading on vortex shedding initiated by the interaction of the rotor bow shock with the stator trailing edge.

Not only do blade row interactions generate loss between a stator and transonic rotor, the size, strength, and trajectory of shed vortices through the rotor passage has been shown by List [18–20] and Nolan [21] to affect rotor pressure ratio and efficiency. Whether the mean vortex path convects near the blade surface or through the center of the rotor blade passage is important.

An understanding of the unsteady phenomena associated with blade loading and axial spacing in turbomachinery will help compressor designers account for unsteady flow physics at design and at a range of operating conditions. Different stator loadings model off-design operating conditions for the stator row. Performance of high-speed, highly loaded turbomachines is very sensitive to operating conditions and off-design performance is very difficult to model and predict.

BLADE-ROW INTERACTION RIG

The Blade Row Interaction (BRI) rig, shown in Fig. 1 was a variation of the AFRL SMI rig [10, 11, 13]. The BRI rig used much of the same hardware with the main difference being the replacement of the blunt, uncambered wake generator of the SMI rig with two upstream stator rows, called the swirler and deswirler. The rotors used in the SMI and BRI rigs were designed for axial inlet flow and, thus, required a swirler and deswirler to maintain axial inlet flow to the rotor. These rows generated a wake by viscous diffusion and the deswirler had a realistic stator trailing edge geometry. As the axial inlet flow passed through the swirler row, a tangential velocity (30 degrees of turning) was introduced to the flow. The stator was highly loaded with a design diffusion factor of 0.45. The design intent was to move the loading as far forward as possible without leading edge separation. Stator loading was changed by adjusting the stagger angle of the swirler which changed the incidence to the deswirler and consequently the suction side boundary layer thickness. Additionally, the swirler row could be clocked relative to the deswirler to control the pitchwise position of the wake from the first blade row and to optimize the total pressure loss at the entrance of the rotor. A stator row downstream of the rotor was also present. The rig was designed to permit the stator-to-rotor axial spacing to be set to three values–"close," "mid," and "far"–as shown in Fig. 1. The average non-dimensional distances between the deswirler trailing edge and the rotor leading edge at the casing are given in terms of the axial distance divided by the mean chord of the deswirler: close spacing 0.23, mid spacing 0.48 and far spacing 1.0.

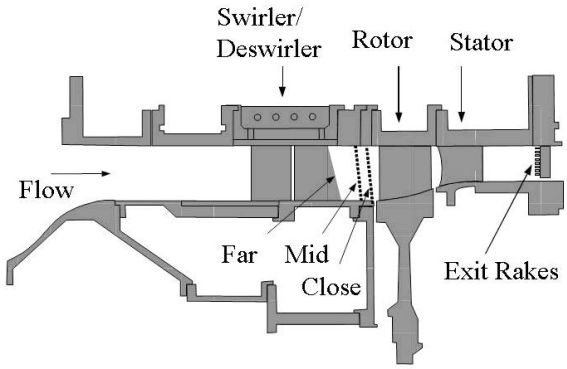

Figure 1. BLADE-ROW INTERACTION (BRI) RIG CROSS SECTION IN ITS GENERAL CONFIGURATION.

Table 1. BRI AERODYNAMIC DESIGN PARAMETERS

Parameter	Deswirler	Rotor	Stator
Number of airfoils	32	28	49
Average aspect ratio	1.24	0.916	0.824
Flow/annulus area $((kg/s)/m^2)$	—	196.30	—
Corrected tip speed (m/s)	—	414.53	—
M_{Rel} LE hub	0.750	1.100	0.830
M_{Rel} LE tip	0.720	1.389	0.700
Max D Factor	0.45	0.545	0.506
LE tip diameter (m)	0.4825	0.4825	0.4825

The design parameters of the BRI rig stage are summarized in Tab. 1. The deswirler chord length and Reynolds number at midspan are 0.04852 m and 5.3×10^5 respectively. It should be noted that the rotor and stator in the BRI rig are different from those used in the SMI rig. Thus, direct performance comparisons between the SMI and BRI rigs should be done with caution. The SMI simulated an embedded transonic core stage, while the BRI rig simulates an embedded fan stage. The major differences between the fan and core stages are fewer rotor blades (28 in the fan versus 33 in the core) and higher tip speed (414.53 m/s in the fan versus 341.37 m/s in the core), resulting in the tip relative Mach number being increased (1.389 versus 1.191) and the hub relative Mach number being transonic (1.100 versus 0.963).

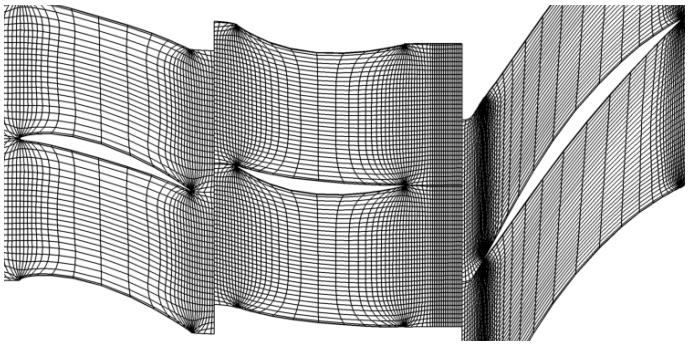

Figure 2. GRID SHOWING TWO BLADE PASSAGES OF EACH ROW AT MIDSPAN (EVERY 6th NODE SHOWN).

NUMERICAL APPROACH

The parallel flow solver TURBO [22] was used to solve the unsteady Reynolds-Averaged Navier-Stokes equations using the NASA/CMOTT k-ε turbulence model [23] specifically developed for turbomachinery flows. The solution algorithm is an iterative, implicit, time-accurate scheme with a modified high order, upwind Roe-scheme spatial discretization. Two layers of subiterations are employed in the code, with the outer layer consisting of a Newton scheme, and the innner layer consisting of symmetric Gauss-Seidel iterations. For this research, periodic quarter annulus simulations were performed to adequately resolve stator-rotor blade row interactions. It should be noted that the fourth blade row, the downstream stator, is not modeled in this simulation, as its inclusion would have resulted in extremely expensive full-annulus simulations rather than quarter annulus periodic simulations.

The TURBO code has been validated on numerous unsteady applications ranging from multistage compressors [24], stall inception [25, 26], distortion transfer [27, 28], blade-row interactions [13, 20, 29], and turbine aerodynamics [30, 31].

Grid Generation

The Turbomachinery Gridding System [32] (TGS) was used for meshing the computational domain. TGS creates block hexahedral H-meshes, with elliptical smoothing at the leading and trailing edges to reduce the effects of the high aspect ratio cells at the blade inlet and exit planes. Grid density increases with each downstream blade row in order to capture unsteady flow features as they propagate downstream. Special consideration was given to the region between the deswirler trailing edge and rotor leading edge in order to adequately resolve rotor bow shocks, shed vortices, and the unsteady interactions of the deswirler and rotor. A sample of the grid showing two blade passages of each blade row for nominal loading at midspan is shown in Fig. 2.

The spatial and temporal resolutions for the simulations match those of List [19], who performed a grid and time step independence study previously. The final node counts are given in Tab. 2 for each blade row. In order to adequately resolve flow features, the node counts match or exceed the recommendations of van de Wall [33]. According to van de Wall, temporal resolution is also important in order to properly resolve vortex formation and propagation through the rotor passage. List [19] found that 320 time steps per blade passing provided a reasonable tradeoff between resources and accuracy, and was sufficient to resolve flow features with these grids.

Table 2. NODE COUNTS FOR EACH BLADE PASSAGE IN THE CURRENT NUMERICAL SIMULATIONS.

	Axial	Radial	Pitch	Passage	Row
8× Swirler	293	101	151	4.5 mil	36 mil
8× Dewirler	361	101	201	7.3 mil	58.4 mil
7× Rotor	391	101	226	8.9 mil	62.3 mil
				TOTAL	153 mil

Numerical Simulations

The computational domain models the first three rows of the BRI test rig as a quarter annulus. Periodic grids with 8 swirler passages, 8 deswirler passages, and 7 rotor passages were generated in order to produce the high fidelity time-accurate simulations. Over 150 million nodes were gridded in each simulation, resulting in hundreds of thousands of CPU hours running in parallel on 500-1000 processors.

The blade loading on the deswirler was changed by varying the stagger angle on the swirler row. Changing the swirler stagger angle changes the incidence on the deswirler, and the resultant loading on the deswirler stator. The highest experimental efficiency was measured at mid spacing at -3.0° stagger. Simulations were performed at mid spacing with three stagger angles of -3.0°, 0.0°, and +1.5°, hereafter referred to as decreased, nominal, and increased loading respectively. These three stagger angles were chosen because they match experimental PIV data [17] and give insight into the effects of increasing stator loading on transonic blade row interactions.

Boundary conditions are consistent with those found in List [19]. The inlet boundary condition was an isentropic inlet condition with the same temperature, pressure, and velocity profiles measured at the inlet of the experimental BRI rig, with an inlet turbulence intensity of 2%. A no-slip condition was imposed at the hub, case, and on each blade surface. The tip clearance gap on the rotor was modeled with 8 cells, allowing for adequate resolution of tip flows as suggested by Van Zante [34]. A hub clearance of 4 cells and a tip clearance of 8 cells was used for the swirler gaps, with the swirler button attachment location ac-

counted for (see Ref. [19]). A sliding interface was imposed at the interface between the deswirler and rotor.

An exit mass flow rate corresponding to peak experimental efficiency for each configuration of the BRI rig was imposed at the rotor exit for each simulation, and convergence is determined by examining the mass flow rates into and out of each blade row. When the inlet and exit mass flow rates for each blade row converge to the imposed exit mass flow rate, the simulation is considered to be converged, and time-averaged and time-accurate solutions are generated for post-processing. Convergence was usually achieved in 12-20 rotor revolutions depending on the simulation. A low-frequency oscillation (likely caused by the exit boundary condition reflecting across the computational domain) in the mass flow rates was present in the simulations, resulting in a periodic behavior in the mass flow rates. This oscillation never decayed completely, but both the time-averaged and time-accurate solutions were generated so as to minimize the effects of the low-frequency oscillation. The time-averaged solutions were taken over a half period of the oscillation, which corresponded to a full rotor revolution. The time-accurate solutions were taken when the mass flow rates for each blade row were closest to the target mass flow.

TIME-AVERAGED RESULTS

The time-averaged efficiencies for each simulation were calculated from the domain inlet and exit mass-averaged temperatures and pressures. The calculated efficiencies were significantly higher than the corresponding experimental efficiencies. List [19] found the same issue with his simulations, and most of the error was attributed to the lack of accounting for the losses incurred in the downstream stator. Another source of error could be the lack of the turbulence model to accurately resolve shear flows in the boundary layers, which is a common difficulty for the k-ε turbulence model [35]. The calculated efficiencies are given in Figure 3 with the corresponding experimentally measured efficiencies at peak performance. Though the magnitudes of calculated efficiency are off by a factor of about 0.95, the same trends in the experimental efficiency are observed in the current simulations at mid spacing. It is remarkable that these high-fidelity simulations were able to capture the same experimentally measured differences in mass flow rate and efficiency between the three loadings, instilling confidence in the simulations. Both experimental and computational results show decreased loading to have the highest efficiency, with nominal loading lower, and increased loading the lowest. It should be noted that the simulation efficiencies in Fig. 3 are scaled by a constant factor of 0.95 in order to show all data points in the same range.

The time-averaged deswirler pressure distribution at midspan was calculated for each simulation and is shown in Fig. 4. The pressure surface distribution is similar for all three loadings. On the suction surface the nominal (0.0°) and increased

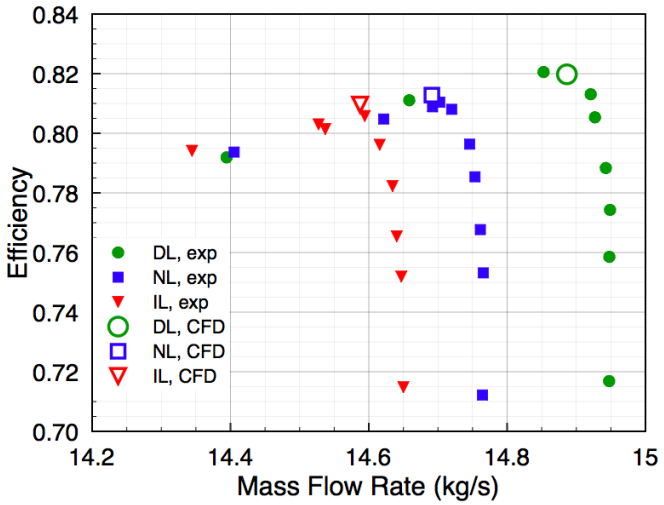

Figure 3. EXPERIMENTAL AND TIME-AVERAGED EFFICIENCES FOR CURRENT SIMULATIONS OF MID SPACING AT DL, NL, AND IL (*NOTE*: CFD EFFICIENCIES SCALED BY 0.95)

loading (+1.5° stagger) profiles are similar. The major difference between those and decreased loading (-3.0° stagger) is the greater flow deceleration between 10% and 40% chord which would generate a thicker boundary layer. At decreased loading the stator is substantially less loaded on the first 20% chord. Integration of C_p over x/C_x yields stator loading values of 0.990, 1.102, and 1.123 for decreased, nominal, and increased loading respectively. This corresponds to an increase from decreased to nominal loading by 11.3%, and from nominal to increased loading by 2.1%.

Analysis of instantaneous blade loading for one quarter rotor revolution showed the greatest loading variation occurred at the pressure surface of the trailing edge, a consequence of the rotor bow shock impacting the stator trailing edge.

TIME-ACCURATE RESULTS

Time-accurate data at midspan was generated for one quarter rotor revolution. This allowed for analysis of approximately 50 rotor blade passings for each simulation. As in other experimental and CFD studies it was observed that vortex shedding was phase-locked with the passing of the rotor bow shock [10–13, 17, 20]. It was verified that the mechanism responsible for causing the vortex formation was a change in unsteady loading on the deswirler caused by the passing rotor bow shock, showing that vortex generation was phase-locked with the rotor passing. Each time the rotor bow shock impacted the deswirler trailing edge a shock-induced vortex formed at the TE and convected downstream.

Examination of the time-accurate data showed large varia-

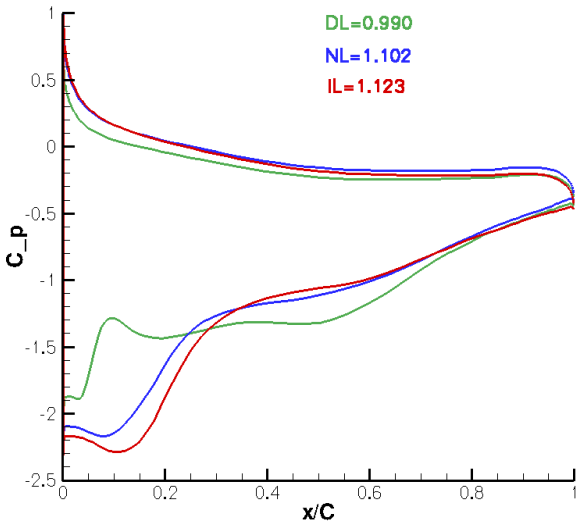

Figure 4. TIME-AVERAGED PRESSURE COEFFICIENT ON DESWIRLER VERSUS CHORD FRACTION AT MIDSPAN.

tions in vortex shedding patterns between the 8 blade passages. Such variation was not be observed in the PIV analysis [17] since images were only obtained at one stator trailing edge. In the experimental PIV analysis of Reynolds [17], a consistent pattern of shed vortices, with three distinct vortices shed per blade passing was observed. In the current simulations it was also observed that a strong vortex was shed due to the passing rotor bow shock. The variation between blade passages is a consequence of the unsteady flow field and shock propagation upstream through the stator passage. This flow non-uniformity will be shown to be a major contributor to the size and strength of shock-induced vortices.

"Normal" Vortex Formation

Figures 5 and 6 illustrate the formation of typical shock-induced vortices at decreased and nominal loading respectively. Velocity contours help to visualize the rotor bow shock as it propagates upstream the deswirler, and radial vorticity contour lines help to visualize both the boundary layers and the vortex formation. We define t/T=0 as the time when the rotor bow shock first interacts with the deswirler TE.

The vortex formation occurs in the following manner as illustrated in Figs. 5 and 6. At t/T=0.125 in Fig. 5 and t/T=0.1875 in Fig. 6 the passing bow shock causes the stator wake to deflect slightly in the direction of the rotor rotation (down). The pressure side boundary layer contains a very strong negative vorticity component, as the steepest velocity gradients are encountered there. The fluid from the pressure side boundary layer flows

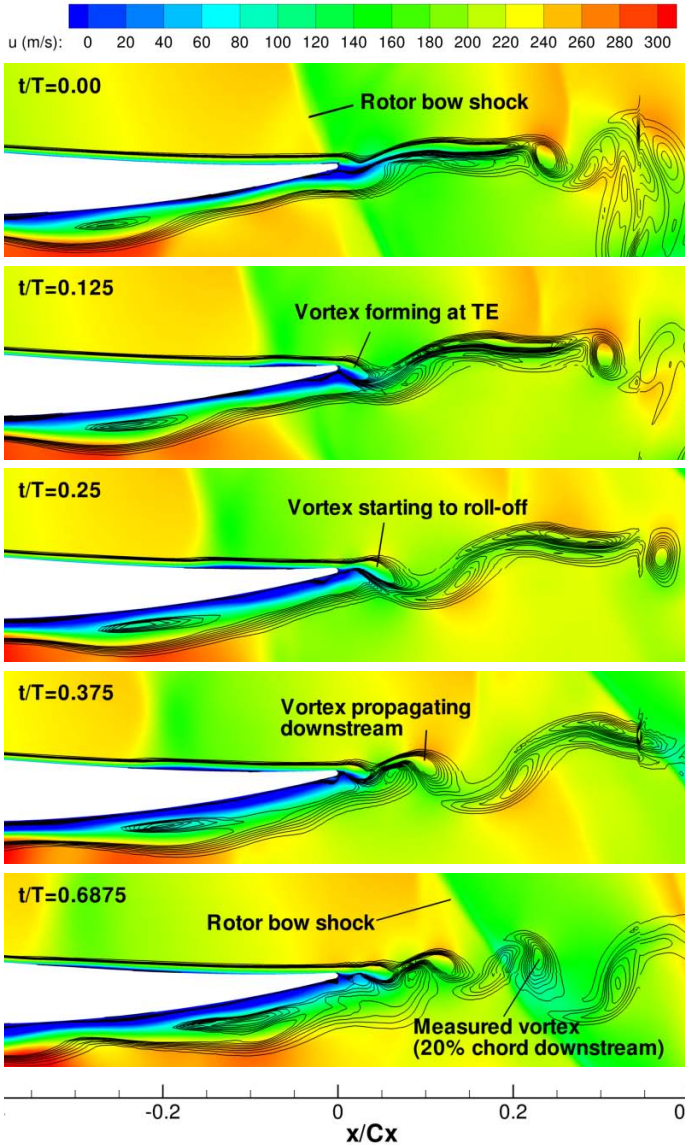

Figure 5. AXIAL VELOCITY CONTOURS WITH RADIAL VORTICITY LINES SHOWING "NORMAL" VORTEX FORMATION ON DESWIRLER TE AT MIDSPAN AT DECREASED LOADING.

downstream, forming a small bubble of strong negative vorticity on the stator trailing edge. The bubble grows in pitch and axial extent until the suction side fluid finally pinches off the vortex, and causes it to roll-off the trailing edge and propagate downstream, as shown at t/T=0.25 in Fig. 5 and at t/T=0.3125 in Fig. 6. At t/T=0.6875 in Fig. 5 and at t/T=0.625 in Fig. 6 the vortex is well-defined near 20% deswirler chord downstream, where vortices were compared for all three loadings.

These vortices will hereafter be referred to as the "normal" vortices. Figure 5 shows a sequence of images illustrating the

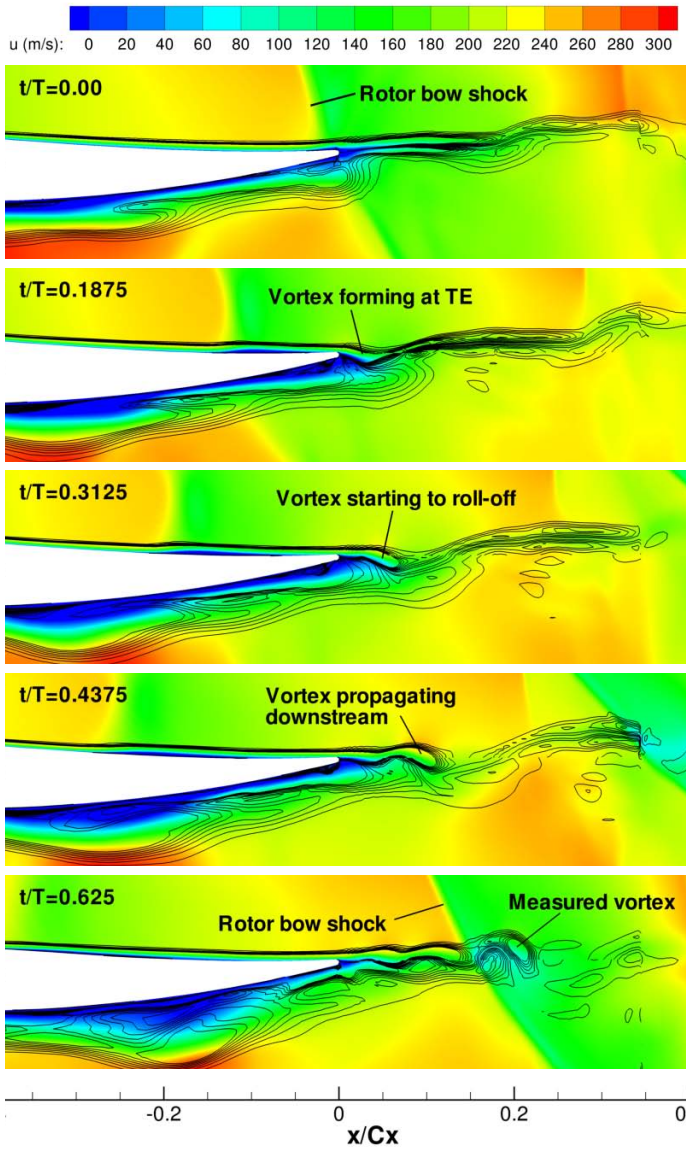

Figure 6. AXIAL VELOCITY CONTOURS WITH RADIAL VORTICITY LINES SHOWING "NORMAL" VORTEX FORMATION ON DESWIRLER TE AT MIDSPAN AT NOMINAL LOADING.

typical formation of a "normal" vortex on the deswirler trailing edge at midspan at decreased loading, and Fig. 6 shows the same for nominal loading. Results from increased loading are similar to nominal loading, and are not shown here. Both image sequences show a comparatively thin SS boundary layer thickness, which was typical for "normal" vortex formation. This allows the higher momentum freestream fluid to help push the shock-induced vortex off the TE before it grows too large, as shown by the small pitchwise extent of the low velocity region at the deswirler TE at t/T=0.25 in Fig. 5 and t/T=0.3125 in Fig. 6.

Vorticity contours were also analyzed for the same sequence of images to help interpret the results shown in Figs. 5 and 6 but are not included here for brevity.

"Large" Vortex Formation

The wake velocity defect on the SS and downstream of TE was observed to have a significant impact on shed vortex strength. Figures 7 and 8 show a different mode of vortex formation for decreased and nominal loading respectively. Here, as the vortices began to form, they were sometimes strengthened by a severe velocity defect in the near-wake region that originated from the SS boundary layer. This is evident from the low velocity region at the SS TE at t/T=0.1875 and 0.3125 in Fig. 7 and at t/T=0.1875 and 0.4375 in Fig. 8. When vortices were seen to form in these regions of severe velocity defect at the TE, the measured strength was significantly higher than that of the "normal" vortices. These vortices will hereafter be referred to as "large" vortices. Figures 7 and 8 show "large" vortices forming on the deswirler TE for decreased and nominal loading respectively. Qualitative differences were not observed between increased and nominal loading, so increased loading is not shown here.

The source or cause of this severe velocity defect region is a periodic thickening of the boundary layer or separation bubble that forms near 40% chord of the stator/deswirler. This phenomena was observed during borescope PIV measurements of the BRI rig [36] which were able to capture both suction and pressure surfaces of the deswirler trailing edge. These numerical simulations [37] as well as those of List [20] have shown such periodic behavior. This occurs when the suction surface boundary layer thickens and sometimes separates when the rotor bow shock propagates upstream. Additional evidence of similar behavior was reported by Sanders and Fleeter [16].

It should be noted that Figs. 5 and 7 contrast the formation of "normal" and "large" vortices at decreased loading while Figs. 6 and 8 contrast "normal" and "large" vortices at nominal loading. The area of low velocity region at the SS and downstream of the TE is much larger and more severe in Figs. 7 and 8, which causes stronger vortices to be shed from the deswirler pressure side. This low velocity region has a large pitchwise extent, as shown in Figs. 7 and 8 at t/T=0.4375, and the low velocity fluid in the SS TE region does not push the vortex downstream quickly, but rather allows the vortex formation to take place over a longer time interval (as noted by the nondimensional time stamp in each image). "Normal" vortices were near 20% chord downstream at t/T=0.6875 and t/T=0.625 in Figs. 5 and 6 respectively, while "large" vortices were not located near 20% chord until the next rotor bow shock was close to interacting with the deswirler TE at t/T=0.9375 in Figs. 7 and 8. This allowed more pressure side boundary layer fluid to be ingested into the "large" vortices before roll-off. This causes these vortices to be significantly larger and stronger than the "normal"

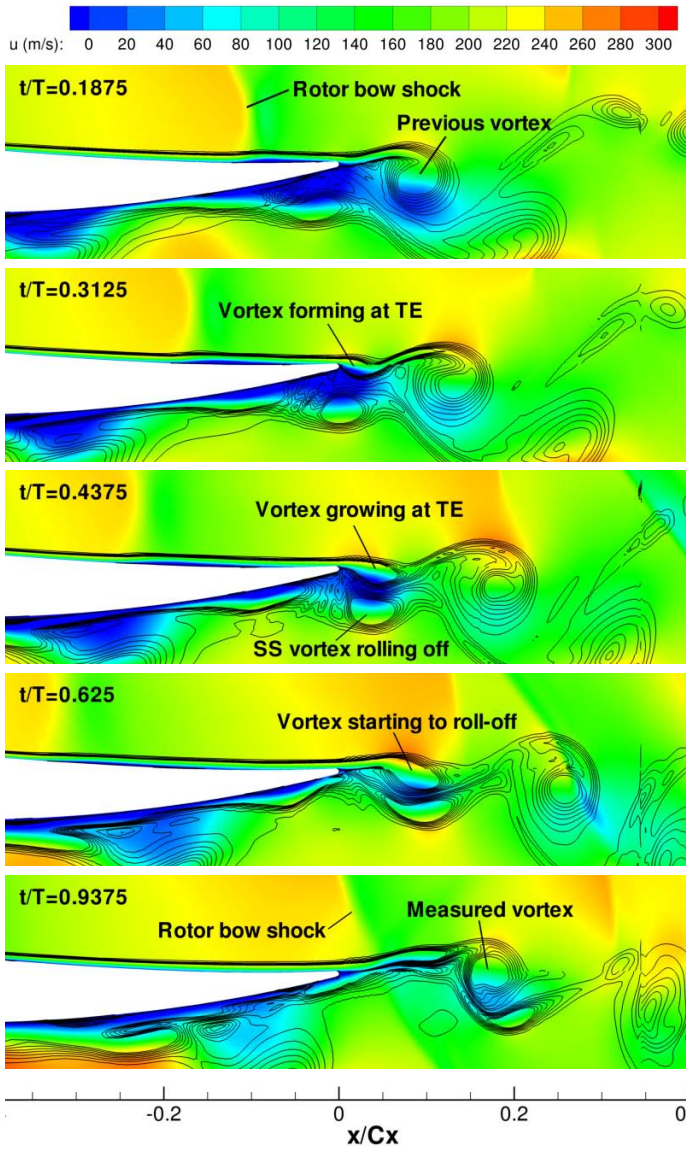

Figure 7. AXIAL VELOCITY CONTOURS WITH RADIAL VORTICITY LINES SHOWING "LARGE" VORTEX FORMATION ON DESWIRLER TE AT MIDSPAN AT DECREASED LOADING.

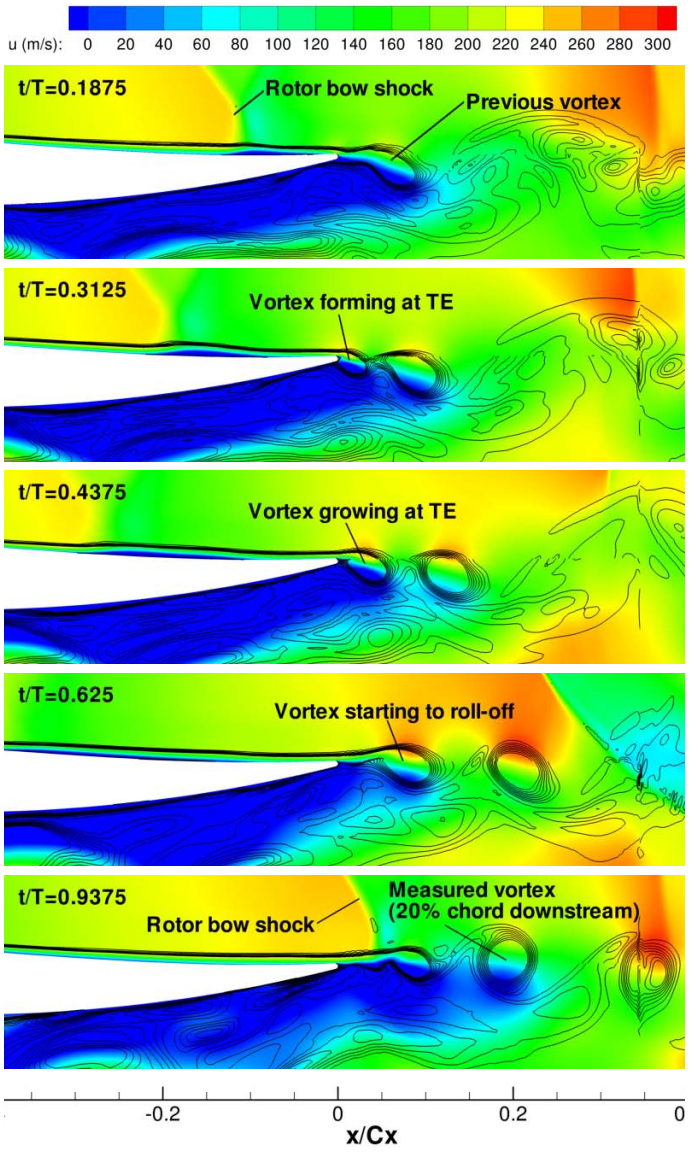

Figure 8. AXIAL VELOCITY CONTOURS WITH RADIAL VORTICITY LINES SHOWING "LARGE" VORTEX FORMATION ON DESWIRLER TE AT MIDSPAN AT NOMINAL LOADING.

vortices which form without the same severe velocity defect.

Circulation

The circulation of each vortex was computed at 20% downstream chord from the line integral of velocity, as shown in Eqtn. 1, for each well-formed vortex observed in the unsteady data in order to quantitatively compare vortices. Vortices were seldom circular, so a non-circular integration path was used at a zero-vorticity contour [17, 38]. The average circulation values for both "normal" and "large" vortices are given in Tab. 3, and are also plotted in Fig. 9.

$$\Gamma = \iint \boldsymbol{\omega} \cdot \mathbf{n}\, dA = \oint \mathbf{u} \cdot dl = \oint U dx + V dy \qquad (1)$$

The average strength of the "normal" shock-induced vortices is nearly constant for all three blade loadings. This suggests that the strength of the "normal" vortices is unaffected by changes in

Table 3. AVERAGE VORTEX STRENGTH FOR SHOCK-INDUCED VORTICES AT MIDSPAN NEAR 20% CHORD DOWNSTREAM.

	Loading	"normal"	"large"
Decreased	0.990	0.437	0.726
Nominal	1.102	0.448	0.866
Increased	1.125	0.432	0.903

stator loading. The "large" vortices are also triggered by the interaction of the shock with the deswirler TE, but are influenced by stator loading effects. Specifically the thickening of the suction surface boundary layer or formation of a separation bubble. As was shown by Reynolds et al. [17], the current results show that vortex strength increases with increased blade loading. In the current simulations it is shown that the increase in "large" vortex strength increases linearly with blade loading, as shown in Fig. 9. As blade loading increased from decreased to nominal loading, an increase of 11%, the measured circulation of "large" vortices increased by 19%. As blade loading increased from nominal to increased loading, an increase of 2%, "large" vortex strength increased by 4%.

The increase in circulation from "normal" to "large" vortices for a given loading also increased with blade loading. Circulation increased from "normal" to "large" vortices by a factor of 1.7 for decreased loading, 1.9 for nominal loading, and 2.1 for increased loading. This implies that there is more variation in vortex strength as loading increases. At decreased loading the vortices were mostly "normal" with the occasional "large" vortex. 24% of the vortices measured at decreased loading were considered "large". At nominal and increased loading there were more "large" vortices than "normal" vortices. At nominal loading the number of "large" vortices increased to 58% of the measured vortices, and at increased loading 54% of the measured vortices were considered "large". As the deswirler loading increases the interaction of the rotor bow shock contributes to the unsteady suction surface boundary layer separation, and causes it to occur more frequently, which results in a greater frequency of "large" vortices.

DISCUSSION OF RESULTS

A thick boundary layer or separation bubble on the suction surface of a stator has been shown to increase the size and circulation of shock-induced vortices formed on the trailing edge of the stator. A stator with higher loading can shed stronger and larger vortices than a stator with lower loading.

Vortex strength can be related to entropy generation through Crocco's Theorem: stronger vortices contain stronger velocity gradients, which generate more entropy as they dissipate, resulting in more loss. This helps explain the experimentally observed decrease in stage performance at increased loading for a given stator-rotor axial spacing.

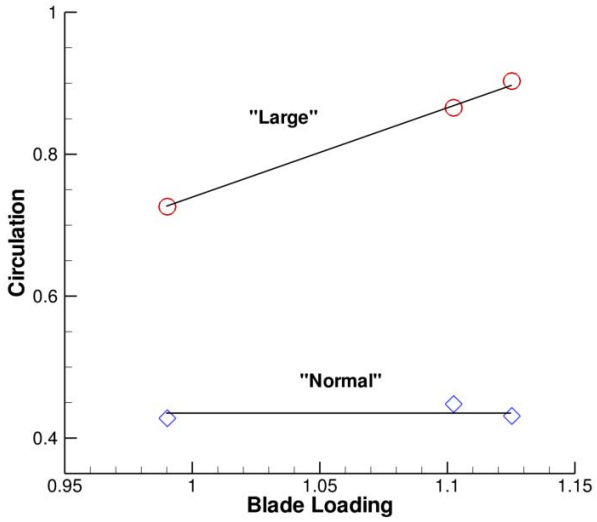

Figure 9. MEASURED VORTEX CIRCULATION FOR "NORMAL" AND "LARGE" SHOCK-INDUCED VORTICES AT ALL THREE LOADINGS. SEE TAB. 3.

This vortex circulation increase can result in increased loss downstream as well. Though the interaction of these stator-shed shock-induced vortices with the rotor bow shock, or their propagation through the rotor passage is not investigated in this research, it is hypothesized that stronger vortices cause further loss downstream. Nolan [21] showed that the upstream stator-shed vortices influence the stagnation pressure distribution that encases the rotor. This affects the loss generation in the rotor boundary layer.

The magnitude of the pitchwise vortex radius has a direct effect on blockage and losses. A larger vortex will cause streamlines to deviate away from axial to go around the vortex, and this process generates additional loss. For highly loaded, high Mach number turbomachines blockage affects the radial distribution of flow, flow swallowing capability of the stage, and flow angles entering and exiting a blade row [39]. In order to improve designs and accurately predict the design and off-design performance of highly loaded, transonic fans and compressors these parameters must be correctly modeled.

CONCLUSIONS

Periodic quarter annulus high-fidelity time-accurate simulations of a single stage transonic compressor were performed on

the BRI rig at mid spacing for decreased, nominal, and increased stator loadings. The simulations have identified the effect loading can have on shock-induced vortex formation as well as what causes the effect. It was found that as the rotor bow shock interacted with the deswirler trailing edge a shock-induced vortex was shed. Two types of shock-induced vortex formation were observed, and the vortex circulation was calculated for both "normal" and "large" vortices. "Normal" vortices were the result of the deswirler geometry, and "large" vortices were due to blade loading effects, though both were triggered by the interaction of the rotor bow shock with the deswirler trailing edge.

"Normal" and "large" vortices formed on the deswirler trailing edge immediately after the shock passing, but the "large" vortices were strengthened at the trailing edge due to a low velocity region at the suction surface. This low velocity region was generated upstream on the suction surface from a shock-induced thickening of the boundary layer or separation bubble. As the shock propagates upstream and reflects through the deswirler passage it causes flow non-uniformities on the blade that can cause suction surface boundary layer separation. When this low velocity region propagates downstream to the trailing edge, it allows vortex formation to take place over a longer time, resulting in more pressure side, negative vorticity fluid to be ingested in the vortex before roll-off. This effect is amplified at increased loading, which causes "large" vortex strength to increase with blade loading. The circulation of the "large" vortex increased 19% when the blade loading increased 11%. The circulation of the "large" vortices was greater than the "normal" vortices by a factor of 1.7, 1.9 and 2.1 at decreased, nominal and increased loadings respectively.

The frequency of "large" vortices increased with blade loading. At decreased loading 24% of measured shock-induced vortices were considered "large". At nominal loading the number increased to 58% of the measured vortices. The interaction of the bow shock with the deswirler trailing edge and consequent reflection and propagation of the shock up the deswirler passage coupled with an increase in stator loading caused the suction surface boundary layer to separate more frequently. This unsteady separation bubble grows and collapses intermittently near mid chord, and as it propagates downstream it affects the vortex shedding characteristics of the stator.

This research has identified and explained how stator loading can have a significant impact on the design and off-design performance of highly loaded, high-speed fans and compressors.

ACKNOWLEDGMENT

The authors would like to thank the Fulton Supercomputing Laboratory at Brigham Young University and the AFRL DoD Supercomputing Resource Center for all their support with this research, including countless millions of computing hours. The authors would also like to thank Michael List for his help with gridding and pre-processing code development.

REFERENCES

[1] Adamczyk, J. J., 2000. "Aerodynamic Analysis of Multistage Turbomachinery Flows in Support of Aerodynamic Design." *ASME Journal of Turbomachinery,* **122**, pp. 189–217.

[2] Hathaway, M. D., Gertz, J. B., Epstein, A. H., and Strazisar, A. J., 1986. "Rotor Wake Characteristics of a Transonic Axial-Flow Fan." *AIAA Journal,* **24**(11), p. 1802.

[3] Kotidis, P. A., and Epstein, A. H., 1991. "Unsteady Radial Transport in a Transonic Compressor Stage." *ASME Journal of Turbomachinery,* **113**, pp. 207–218.

[4] Van de Wall, A. G., Kadambi, J. R., Boyle, R. J., and Adamczyk, J. J., 1996. "The Transport of Vortices Through a Turbine Cascade." *ASME Journal of Turbomachinery,* **118**(4), pp. 654–662.

[5] Smith, L. H., 1966. "Wake Dispersion in Turbomachines." *ASME Journal of Basic Engineering*(3), pp. 668–690.

[6] Mikolajczak, A. A., 1977. "The Practical Importance of Unsteady Flow." *Unsteady Phenomena in Turbomachinery*(AGARD CP-144).

[7] Smith, L. H., 1993. "Wake Ingestion Propulsion Benefit." *AIAA Journal of Propulsion and Power,* **9**(1), pp. 74–82.

[8] Deregal, P., and Tan, C. S., 1996. "Impact of Rotor Wakes on Steady-State Axial Compressor Performance." ASME Paper 96-GT-253.

[9] Van Zante, D. E., Adamczyk, J. J., Strazisar, A. J., and Okiishi, T. H., 2002. "Wake Recovery Performance Benefit in a High-Speed Axial Compressor." *ASME Journal of Turbomachinery,* **124**, pp. 275–284.

[10] Gorrell, S. E., Copenhaver, W. W., and Chriss, R. M., 2001. "Upstream Wake Influences on the Measured Performance of a Transonic Compressor Stage." *AIAA Journal of Propulsion and Power,* **17**, pp. 43–48.

[11] Gorrell, S. E., Okiishi, T. H., and Copenhaver, W. W., 2003. "Stator-Rotor Interactions in a Transonic Compressor, Part 1: Effect of Blade-Row Spacing on Performance." *ASME Journal of Turbomachinery,* **125**, pp. 328–335.

[12] Gorrell, S. E., Okiishi, T. H., and Copenhaver, W. W., 2003. "Stator-Rotor Interactions in a Transonic Compressor, Part 2: Description of a Loss Producing Mechanism." *ASME Journal of Turbomachinery,* **125**, pp. 336–345.

[13] Gorrell, S. E., Car, D., Puterbaugh, S. L., Estevadeordal, J., and Okiishi, T. H., 2006. "An Investigation of Wake-Shock Interactions with Digital Particle Image Velocimetry and Time-Accurate Computational Fluid Dynamics." *ASME Journal of Turbomachinery,* **128**(4), pp. 616–626.

[14] Langford, M. D., Breeze-Stringfellow, A., Guillot, S. A., Solomon, W., Ng, W., and Estevadeordal, J., 2007. "Experimental Investigation of the Effects of a Moving Shock

Wave on Compressor Stator Flow." *ASME Journal of Turbomachinery,* **129**(1), pp. 127–135.

[15] Ottavy, X., Trebinjac, I., and Voullarmet, A., 2001. "Analysis of the Interrow Flow Field Within a Transonic Axial Compressor: Part 1 - Experimental Investigation." *ASME Journal of Turbomachinery,* **123**, pp. 49–56.

[16] Sanders, A., and Fleeter, S., 2000. "Experimental Investigation of Rotor-Inlet Guide Vane Interactions in Transonic Axial-Flow Compressor." *AIAA Journal of Propulsion and Power,* **16**, pp. 421–430.

[17] Reynolds, S. B., Gorrell, S. E., and Estevadeordal, J., 2010. "PIV Analysis on the Effect of Stator Loading on Transonic Blade-Row Interactions." ASME Paper GT2010-22576.

[18] List, M. G., Gorrell, S. E., Turner, M. G., and Nimersheim, J. A., 2007. "High-fidelity Modeling of Blade Row Interaction in a Transonic Compressor." AIAA Paper 2007-5045.

[19] List, M. G., 2007. "Quarter annulus simulations of blade row interactions at several gaps and discussion of flow physics." Master's thesis, University of Cincinnati, Cincinnati, OH, August.

[20] List, M. G., Gorrell, S. E., and Turner, M. G., 2010. "Investigation of Loss Generation in an Embedded Transonic Fan Stage at Several Gaps Using High-fidelity, Time-accurate Computational Fluid Dynamics." *ASME Journal of Turbomachinery,* **132**(011014), January.

[21] Nolan, S. P. R., Botros, B. B., Tan, C. S., Adamczyk, J. J., Greitzer, E. M., and Gorrell, S. E., 2009. "Effects of Upstream Wake Phasing on Transonic Axial Compressor Performance." ASME Paper GT2009-59556.

[22] Chen, J. P., and Briley, W. R., 2001. "A Parallel Flow Solver for Unsteady Multiple Blade Row Turbomachinery Simulations." ASME Paper 2001-GT-348.

[23] Zhu, J., and Shih, T. H., 2000. CMOTT Turbulence Module for NPARC Contract Report NASA CR 204143, NASA Glenn Research Center, Lewis Field, OH.

[24] Van Zante, D., Chen, J., Hathaway, D., and Chriss, R., 2008. "The Influence of Compressor Blade Row Interaction Modeling on Performance Estimates from Time-Accurate, Multistage, Navier-Stokes Simulations." *ASME Journal of Turbomachinery,* **130**(1), January.

[25] Chen, J. P., Hathaway, M. D., and Herrick, G. P., 2008. "Prestall behavior of a transonic axial comrpessor stage via time-accurate numerical simulation." *ASME Journal of Turbomachinery,* **130**(4), October.

[26] Chen, J. P., Webster, R. S., Hathaway, M. D., Herrick, G. P., and Skoch, G. J., 2006. "Numerical Simulation of Stall and Stall Control in Axial and Radial Compressors." AIAA Paper 2006-418.

[27] Gorrell, S. E., Yao, J., and Wadia, A. R., 2008. High Fidelity URANS Analysis of Swirl Generation and Fan Response to Inlet Distortion *AIAA paper 2008-4985*, 44th AIAA/ASME/SAE/ASEE Joint Propulsion Conference & Exhibit, Hartford, CT, July.

[28] Yao, J., Gorrell, S. E., and Wadia, A. R., 2008. "High-Fidelity Numerical Analysis of Per-Rev-Type Inlet Distortion Transfer in Multistage Fans - Part II: Entire Component Simulation and Investigation" ASME Turbo Expo 2008: Power for Land, Sea and Air, June 2008, Berlin, Germany GT2008-50813.

[29] Turner, M. G., Gorrell, S. E., and Car, D., 2005. "Radial Migration of Shed Vortices in a Transonic Rotor Following a Wake Generator: A Comparison Between Time Accurate and Average Passage Approach." ASME Paper GT2005-68776.

[30] Shyam, V., Ameri, A., Luk, D. F., and Chen, J. P., 2011. "3D Unsteady Simulation of a Modern High Pressure Turbine Stage Using Phase Lag Periodicity: Analysis of Flow and Heat Transfer." *ASME Journal of Turbomachinery,* **133**(031015), July.

[31] Southworth, S. A., Dunn, M. G., Haldeman, C. W., Chen, J. P., Heitland, G., and Liu, J., 2009. "Time-Accurate Predictions for a Fully Cooled High-Pressure Turbine StagePart I: Comparison of Predictions With Data." *ASME Journal of Turbomachinery,* **131**(031003), July.

[32] Kamp, M. A., Nimersheim, J., Beach, T., and Turner, M. G., 2007. "A Turbomachinery Gridding System." *AIAA Paper 2007-18*.

[33] van de Wall, A., Breeze-Stringfellow, A., and Dailey, L., 2006. "Computational Investigation of Unsteady Flow Mechanisms in Compressors with Embedded Supersonic Rotors." ASME Paper GT2006-90633.

[34] Van Zante, D. E., Strazisar, A. J., Wood, J. R., Hathaway, M. D., and Okiishi, T. H., 2000. "Recommendations for Achieving Numerical Simulation of Tip Clearance Flows in Transonic Compressor Rotors." *ASME Journal of Turbomachinery,* **122**, pp. 733–742.

[35] Wilcox, D. C., 1998. *Turbulence Modeling for CFD*. DCW Industries, Inc., La Cañada, CA.

[36] Estevadeordal, J., Gorrell, S., and Puterbaugh, S., 2008. "PIV Measurements of Blade-Row Interactions in a Transonic Compressor for Various Operating Conditions." AIAA Paper 2008-4700.

[37] Clark, K. P., and Gorrell, S. E., 2011. "Time-Accurate CFD Analysis on the Effects of Upstream Stator Loading and Blade Row Interactions on Stator Suction Side Boundary Layer Behavior." AIAA Paper 2011-303.

[38] Raffel, M., Willert, C. E., and Kompenhans, J., 1998. *Particle Image Velocimetry*. Springer.

[39] Turner, M. G., Norris, A., and Veres, J., 2003. "High Fidelity 3D Simulation of the GE90." AIAA Paper 2003-3996.